

CFD simulation of a vortex-controlled diffuser for a jet engine burner

ARTICLE INFO

Received: 11 April 2023
Revised: 10 July 2023
Accepted: 23 August 2023
Available online: 11 September 2023

A computational flow analysis of an ideal vortex-controlled diffuser (VCD) was carried out. The simulation model used is the compressible Reynolds averaged Navier-Stokes equations (RANS), with the application of the RNG based k-ε turbulence model. The effects of important parameters like static pressure recovery, bleed fraction, position of bleed slot, have been studied and comparisons were made with respect to VCD without the bleed configuration and the following features were revealed: radial profiles of velocity at inlet, mid-planes and exit planes, including diffuser effectiveness (i.e. static pressure recovery), diffuser efficiency, reattachment length and diffuser total pressure loss. Results obtained by applying the RNG turbulence model show an instantaneous improvement in the diffuser efficiency that happen at reasonably minimal suction rates. From the calculations, it has been verified and shown in the analysis that the effect of the bleed positioning offers advantages in relation to where it is located.

Key words: vortex-controlled diffuser, bleed slot, modelling, static pressure recovery, reattachment length

This is an open access article under the CC BY license (<http://creativecommons.org/licenses/by/4.0/>)

1. Introduction

Huge advancements, in recent years, in the technology of different components of aircraft turbines have increased the focus on the need for the design and manufacture of short, effective diffusers suitable to be installed between the compressor and combustor and having the main goal of reducing air velocity to guarantee efficient combustion with a minimal pressure loss.

When a compressor exit velocity increases, the diffuser then needs to compensate by having higher ratio of cross sectional area as to achieve proper mixing and flow conditions for good performance and the use of annular combustors results in lower pressure losses due to their design features, with that said, it's very important to ensure adequate mixing at the diffuser outlet to maintain optimal performance characteristics.

A vortex controlled diffuser allows for precise adjustment of the pressure within specific regions of rapidly expanding fluid flows using small gaps. Heskestad is credited with originating this idea [9]. In his work, the incorporation of edge suction that was fitted at the edge of the curved surface helped to channel the flow to a border in a way that considerably shorten the length of the recirculation zone. Heskestad [8] also did an investigation on edge suction at the step expansion of a circular pipe, analyzing the usefulness of the structure for a short diffuser. Here, he applied a consistent inlet profile with a fine boundary layer. He indicated that the structural design of the suction slot in addition to the suction rate, affected the flow expansion. He emphasized that suction power should be taken in to factor while evaluating the diffuser's effectiveness.

The need for the manufacture of efficient diffuser to be placed between the compressor and combustor was the driving force behind the continued evolution of the vortex controlled diffuser (VCD) design.

Adkins [2] collected data using a variety of tubular and annular research diffusers with inflow to outflow cross sectional area ratios between 1.9:1 to 3.2:1 and with diffus-

er inlet Mach numbers and velocity-profile displacement levels that were similar to those found in engine systems. He discovered that, for modest bleed rates, diffuser lengths just 1/3 of those needed for conventional conical diffusers may be used to reach efficiencies of more than 80%. Later, Adkins studied a hybrid diffuser, which combines a VCD with

a traditional diffuser [1]. According to his findings, bleed rates were lower than those needed for the step VCD setups that had previously been researched.

The VCD's mode of operation is yet unknown. A possible theory suggests that the bleed gap creates a zone of high shear, which causes a layer of strong turbulence to condense downstream and prevent flow separation along the outer wall [2]. Others have asserted that the principal impact of suction is to merely bend or redirect the mean flow around the acute corner, shortening the recirculation region [10]. In a fluid diffusion system, the fluid naturally has the propensity to detach off the walls of the widening tunnel, change course, and stream backward toward the direction of the negative pressure [7].

In this current paper, the performance of an ideal VCD was carried out numerically. The geometry and mesh was structured using Gambit software and ANSYS FLUENT 14 used for the flow simulation. The flow simulation used the compressible Reynolds averaged Navier-Stokes equations (RANS), with application of the renormalization group (RNG) based k-ε turbulence model. The presented results describes the effects of the bleed rates applied, ranging from 0%, 1%, 1.2%, and 2%.

The findings from the diffuser with no suction configuration were provided for purposes of comparison. The velocity profiles, plots of velocity contours, static pressure rise, and pressure recovery coefficient were used to illustrate and analyze the flow structure in detail.

Chakrabarti et al. [4, 13] performed a computational simulation of a diffuser sudden expansion with fence for low Reynolds number regime and concluded that, at the

point of the neck region, a wall incorporated in a sudden expansion design affects how the flow diffuses and that a quick fence enlargement does not necessarily result in more benefits at a lower fence subtended angle (FSA) when Reynolds numbers are smaller. Aside from being reliant on Reynolds number, the average static pressure rise normally relies on the fence's location relative to the throat as well as its defined angle.

The application of multistep configuration of a sudden expansion diffuser at low Reynolds numbers provides important advantages, although there's no significant improvement in its efficiency at larger Reynolds number flow [14].

There are two primary styles of annular diffusers utilized in gas turbine combustion engines to reduce the speed of fluids, a faired and dump diffuser, both diffusers have long been a common component of aero-engine combustion. Dump diffusers have become commonly adopted due to their greater resilience to fluctuations in inflow velocity patterns and component dimensions [11, 12].

The investigation done on a dump diffuser [19], explained that, since the airspeed dispersion at the diffuser exit is inconsistent, the bleed flow through the dump location helps the dump diffuser work better and the ideal bleed rate is between 0.4 and 0.7 percent. It has been discovered that the ideal inlet vortex level and prediffuser angles are required to get an optimum static pressure recovery. Particularly for a little prediffuser angles, the dump gap prove to have a substantial impact on the static pressure recovery [6].

2. Research objectives

The objectives of this research are listed as follows:

- to give more information on the physical processes that accounts for the efficiency attained by the VCD
- to observe and analyze how the design of the vortex chamber affected diffuser effectiveness while changing the radial and axial positioning of the bleed slot X and Y respectively (see Fig. 1)
- to see how the RNG-based k-ε – model outperforms the traditional k-ε model at predicting difficult flow recirculation of this nature
- to collect and analyze the flow characteristics and properties derived from the computations.

Computational viewpoints of the present work

The computational analysis of a vortex-controlled diffuser (VCD) was performed in this paper. The calculations were done with RNG based k-ε model with enhanced wall functions. Bleed gap effects and the vortex chamber on the diffuser performance was investigated numerically. The following are the lists of certain characteristics and criteria that were taken into account:

- reattachment length, L_R
- separation of the flow within the diffuser
- pressure recovery coefficient.

3. Numerical methodology

The computational approach adopted for this research work is the compressible RANS equations suitable for motion calculation and explanation inside a traditional axisymmetric VCD setup. The mathematical model for instan-

aneous continuity (1), momentum (2) and energy (3) for compressible fluid are as follows:

$$\frac{\partial \bar{\rho}}{\partial t} + \frac{\partial}{\partial x_j} (\bar{\rho} \hat{u}_j) = 0 \quad (1)$$

$$\frac{\partial}{\partial t} (\bar{\rho} \hat{u}_i) + \frac{\partial}{\partial x_j} (\bar{\rho} \hat{u}_j \hat{u}_i) = - \frac{\partial p}{\partial x_i} + \frac{\partial \bar{\sigma}_{ji}}{\partial x_j} + \frac{\partial \tau_{ji}}{\partial x_j} \quad (2)$$

$$\begin{aligned} \frac{\partial}{\partial t} (\bar{\rho} \hat{E}) + \frac{\partial}{\partial x_j} (\bar{\rho} \hat{u}_j \hat{H}) &= \frac{\partial}{\partial x_j} (\bar{\sigma}_{ji} \hat{u}_i + \overline{\sigma_{ji} u_i''}) \\ - \frac{\partial}{\partial x_j} (\bar{q}_j + c_p \overline{\rho u_j'' T''} - \hat{u}_i \tau_{ji} + \frac{1}{2} \overline{\rho u_i'' u_i''}) & \end{aligned} \quad (3)$$

where u_i and x_i represents velocity components, p stands for pressure, ρ is the fluid density and τ_{ji} is the viscous stress tensor, \bar{q}_j is the heat flux vector, \hat{E} is the total energy per unit mass, and \hat{H} is the total enthalpy per unit mass. Specifically,

$$\hat{E} = \hat{e} + \frac{1}{2} \hat{u}_i \hat{u}_i \quad (4)$$

$$\hat{H} = \hat{h} + \frac{1}{2} \hat{u}_i \hat{u}_i - \hat{e} + \frac{\bar{p}}{\rho} + \frac{1}{2} \hat{u}_i \hat{u}_i \quad (5)$$

$$\bar{q}_j = - \overline{k_T \partial T / \partial x_j} \approx - \frac{c_p \hat{\mu}}{Pr} \frac{\partial \hat{T}}{\partial x_j} \quad (6)$$

where \hat{e} and \hat{h} , represents internal energy and enthalpy per unit mass respectively.

The viscous stress term is:

$$\bar{\sigma}_{ji} \approx 2 \hat{\mu} \left(\hat{S}_{ji} - \frac{1}{3} \frac{\partial \hat{u}_k}{\partial x_k} \delta_{ji} \right) \quad (7)$$

The Reynolds stress term $\tau_{ji} \equiv - \overline{\rho u_j'' u_i''}$, has a negative sign and the density can occasionally be omitted from the formulation, however, it is irrelevant if the terms are used differently as long as the expression is consistent all through the derivation. The term c_p is the heat capacity at constant pressure, and Pr is the Prandtl number which for air is approximately 0.72. The overline represents the standard average mean time, the averaging time scale is long for turbulent fluctuations, and short for unsteady mean flow. Using Sutherland's Law will help to compute the dynamic viscosity $\hat{\mu}$, which gives a relationship between the dynamic viscosity and the temperature of an ideal gas [17]. By entering the local value of temperature (T) into equation (8), Sutherland's Law can be used to calculate the local value of dynamic viscosity:

$$\mu = \mu_0 \left(\frac{T}{T_0} \right)^{3/2} \left(\frac{T_0 + S}{T + S} \right) \quad (8)$$

where T , is the temperature and μ_0 , T_0 , and S are constants, $\mu_0 = 1.716 \times 10^{-5}$ kg/(ms), $T_0 = 491.6$ Rankine ($^{\circ}R$), and $S = 198.6$ Rankine ($^{\circ}R$).

To close this system, its necessary to specify equation of state:

$$\bar{p} = (\gamma - 1) \left[\bar{\rho} \hat{E} - \frac{1}{2} \bar{\rho} (\hat{u}^2 + \hat{v}^2 + \hat{w}^2) - \bar{\rho} k \right] \quad (9)$$

where k represents local turbulent kinetic energy:

$$k = \frac{1}{2} [(\hat{u}_i'')^2 + (\hat{v}_i'')^2 + (\hat{w}_i'')^2].$$

Below Favre-averaged mathematical terms need to be approximated: τ_{ji} ; $c_p \overline{\rho u_j'' T''}$; $\overline{\sigma_{ji} u_i''}$; and $\frac{1}{2} \overline{\rho u_i'' u_i''}$.

Reynolds stress terms (τ_{ji}) are the main subject in most turbulence calculations. The Reynolds-stress tensor is a symmetric tensor ($\tau_{ji} = \tau_{ij}$), and thus it has six independent components that have to be modelled. Therefore to solve Eq. (2), it is necessary to find enough equations to close the system.

The tensor is modelled using the Boussinesq approximation [18], thus the Reynolds stress tensor is given by:

$$\tau_{ji} = 2\hat{\mu}_t \left(\hat{S}_{ji} - \frac{1}{3} \frac{\partial \hat{u}_k}{\partial x_k} \delta_{ji} \right) - \frac{2}{3} \bar{\rho} k \delta_{ij} \quad (10)$$

$$\hat{S}_{ji} = \frac{1}{2} \left(\frac{\partial u_i}{\partial x_j} + \frac{\partial u_j}{\partial x_i} \right) \quad (11)$$

where $\hat{\mu}_t$ – represents eddy viscosity, \hat{S}_{ji} – represents strain-rate tensor, k – represents the specific kinetic energy, ρ – the density, the operator δ_{ij} – is the Kronecker delta.

Equation (12) describes the turbulent heat flux model:

$$c_p \overline{\rho u_j'' T''} \approx - \frac{c_p \hat{\mu}_t}{Pr_t} \frac{\partial \hat{T}}{\partial x_j} \quad (12)$$

where Pr_t stands for turbulent Prandtl number, having a constant number around 0.9 for air. Different models are used to represent the terms associated with turbulent transport and molecular diffusion in the energy equation. For instance:

$$\overline{\sigma_{ji} u_i''} - \frac{1}{2} \overline{\rho u_j'' u_i'' u_i''} \approx \left(\hat{\mu} + \frac{\hat{\mu}_t}{\sigma_k} \right) \frac{\partial k}{\partial x_j} \quad (13)$$

where σ_k is a coefficient associated with the modeling equation for k .

3.1. Turbulence model

Unsteady velocity fields are a defining characteristic of turbulent flows. The unsteady flow would combine with transported quantities such as momentum, energy, and species concentration, causing the transported quantities to fluctuate as well. The Reynolds stress turbulence model is implemented in the program. The choice of the k - ε model is dictated by the calculation time and the recommendations of the k - ε model for the analyzed class of flows.

3.2. The RNG k - ε model

Previous experiments have pointed out that the RNG based models does yield results that are preferable to those of the conventional k - ε model in relation to boundary layer, extreme strained, separated and high laminar bending flows [16].

The instantaneous Navier-Stokes equations are used to develop the RNG-based k - ε turbulence model by employing the RNG computational method. The RNG model has an extra component in its ε calculation that considerably increases the reliability for unsteady shear flows. Only turbulent areas along a radial plane that are not closed to the wall are suitable for the k - ε models. High Reynolds number turbulent flow requires a separate wall modeling to connect the 100% turbulent state and the close to the wall frictional zone. In order to depict flow characteristics like separation effectively, the near wall region must be adequately structured.

4. Computational investigation of the vortex-controlled diffuser (VCD)

The fundamental objectives of this work was to clarify the governing flow mechanics of a VCD by altering the values of the radial and axial distance Y , X respectively (see Fig. 1). The examination initially focuses on the bleed effectiveness and the reattachment mechanism. In order to compare and achieve these objectives, flow simulations were conducted for a basic, 2D VCD without a bleed configuration (Fig. 2). When performing such CFD calculation, it's crucial to make sure the result is realistic within the parameters of the model assumptions employed and grid independent. The basic 2D VCD study would help to:

- develop a grid-based solution
- evaluate the effectiveness of the turbulent model
- apply and check for suitable boundary conditions
- achieve grid independence.

After the study, the concluded methodology was then maintained throughout the CFD analysis, and covering its findings reported in the subsequent chapters.

4.1. Flow domain arrangement

The structure of the VCD with and without the bleed configuration were created using “GAMBIT” modeling software (see Fig. 1 and 2), the inlet diameter is 0.031 m, the overall area ratio is 1.612 and a non-dimensional length. Only half of the geometry is taken into account (an axisymmetric flow calculation). The two-dimensionality allows an axisymmetric boundary condition at mid inlet duct height, where by reducing both the computing effort and the number of grid cells in half.

Referring to Fig. 1, is a primary duct positioned in a secondary duct, with a structured vortex fence placed in the secondary duct downhill of the primary duct's outlet, a bleed duct used for the air pressure regulation is located within the secondary duct. when a little passage of air is allowed using the bleed duct, it enables the incoming stream of air from the primary duct to diffuse quickly, receiving substantially smaller amounts of air in the secondary duct. The velocity of the inflow air is changed by altering the rate of bleed flow, which changes the quantity of air that travels down the secondary duct.

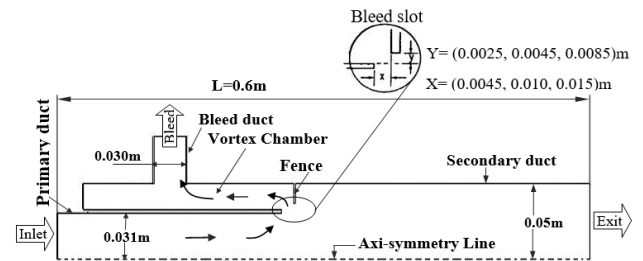


Fig. 1. Vortex-controlled diffuser (VCD) computational domain, with the bleed configuration

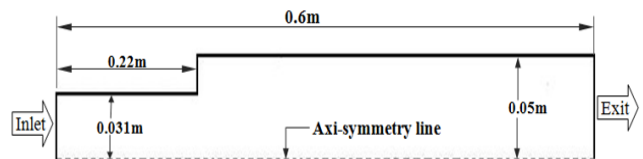


Fig. 2. Fluid domain of the VCD with no bleed configuration

4.2. Computational grid

The fluid flow area was meshed after the VCD models were generated. A multi-block structural mesh was created with a boundary layer close to the recirculation region from the step as shown in Fig. 3 and 4, boundary layer meshing was applied in order to handle the strong velocity fluctuations and for better visualization of fluid characteristics around this region.

4.3. Grid sensitivity study

A detailed grid-independent investigations have been conducted with the goal to choose the appropriate grid size by adjusting the node spacing on the edges and utilizing the standard mesh law approach. The first order discretization methods, the RNG k-ε model, and enhanced wall functions were used to study the grid-independence employing three different sizes of grids. As the mesh size decreases, the more fine mesh is obtained, providing best results and the length of recirculation increases as the mesh size is increased. Table 1 shows the three tested mesh sizes.

Table 1. Three tested mesh sizes

Grid No.	Mesh	Element Type	No. of Cells	No. of Face	No. of Nodes
1.	Coarse mesh (No boundary layer)	Quad.	1985	4149	2165
2.	Fine mesh	Quad.	3064	6333	3270
3.	Finer mesh	Quad.	4782	9846	5065

Grid independence was checked on the static pressure recovery as depicted in Fig. 5, we can observe that the calculation with grid number 2 indicates little change in the static pressure rise compared to the result from grid number 3. Hence, further grid refinement seems unnecessary. Grid number 2 was used for the present analysis.

Streamline plots of velocity magnitude for every grid generated are depicted in Fig. 6, it illustrates the variations in the recirculation flow development and flow reattachment lengths, L_R .

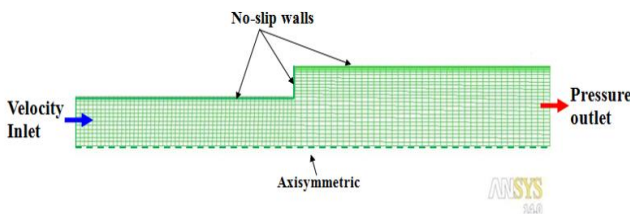


Fig. 3. VCD computational grid, with no bleed configuration

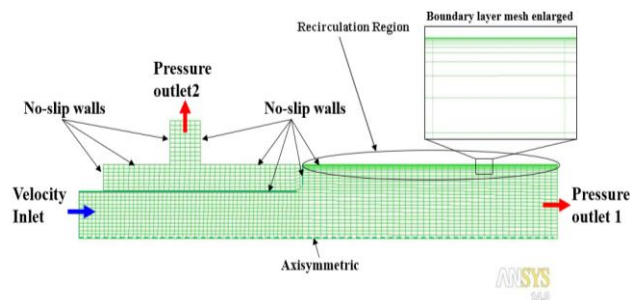


Fig. 4. VCD computational grid, with the bleed configuration (boundary layer near the recirculation region)

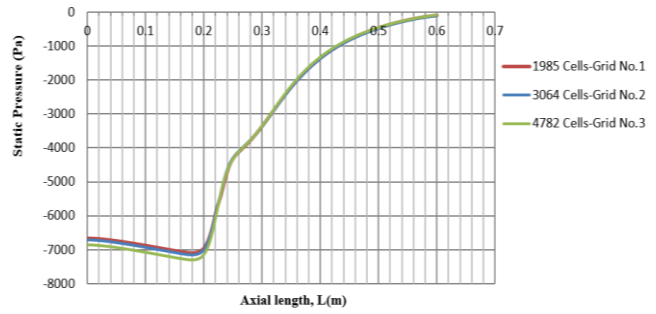


Fig. 5. Static pressure recovery for different set of grids

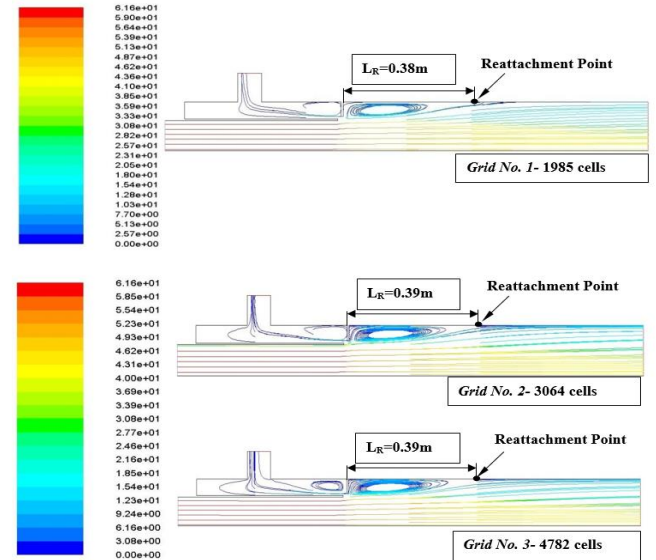


Fig. 6. Velocity streamlines at reattachment length, L_R for all set of grids in grid independence study (RNG k-ε model, Enhanced wall function, First order discretization schemes, for 1% Bleed)

A thorough understanding of the turbulent flow behavior, particularly fluctuations of the principal recirculation zone's reattachment length was offered by Schäfer [15], it was explained that the erratic shear layers separating the principal flow and the recirculation waves contain vertical patterns that cause the immediate reattachment and the secondary separation line to flutter.

4.4. Boundary conditions

Table 2 shows summary of the boundary conditions and the numerical method implemented for RNG k-ε model. Five types of boundary conditions were specified during the flow setup, which includes Inlet, Outlet, Bleed duct, Wall and Axi-symmetry constraints.

Inlet: In the current computation, velocity was set at 60 m/s as the inflow constraint with a flat profile, this value was applied in the two configured diffusers, the hydraulic diameter at the inlet is given as 0.0589 m. A predetermined level of turbulence or 1% of the corresponding flow diameter was used, therefore the turbulent intensity was set at, $I = 0.16(Re_{DH})^{-1/8}$, where Re_{DH} is the Reynolds number based on the hydraulic diameter.

Outlet: A pressure outlet having a zero pressure gauge has been selected as the outlet boundary constraint.

Bleed duct: Pressure outlet boundary constraints is specified at the bleed duct. This duct is in vertical position, therefore a negative uniform pressure was applied. The bleed rates are equal to 0%, 1%, 1.2% and 2% of the operating pressure (1 MPa).

Wall: The entire wall were applied a non-slip surface criteria. To avoid the effects of wall friction, a default friction constant, 0.5 was applied which represents a uniform sand grain roughness.

Axi-Symmetry: The computation solely addresses the top half of the geometry, an axi-symmetric boundary constraints were assigned to both generated models on the symmetry plane, and a higher-order scheme was used. The residuals of all parameters were kept in the order of 10^{-6} in the convergence solution.

The motion of fluids on each side of the mirror plane border condition is subject to restrictions known as "mirroring" conditions, i.e. the normal velocity vector is zero at the border of the symmetry axis [3].

Table 2. The list of applied flow constraints, including numerical method implemented for RNG k- ϵ model

CASE	RNG
Model	Steady, two dimensional compressible
Turbulence model	RNG k- ϵ (2 equation)
MATERIALS	
Density	Ideal-gas
Viscosity	$\mu = 1.7894 * 10^{-5}$ kg/ms
DISCRETIZATION	
Pressure	Standard
Pressure-velocity coupling	SIMPLE
Momentum	First order upwind
Turbulent kinetic energy	First order upwind
Turbulent dissipation rate	First order upwind
Energy	First order upwind
BOUNDARY CONDITIONS	
Inlet	
Velocity components, (method- magnitude and direction)	Assumed velocity 60 m/s and temperature 500 K
Turbulence intensity	Tu = 1%
Hydraulic diameter	$D_H = 0.0589$ m
Outlet	
Outlet pressure	Gauge pressure (Pascal) = 0
Backflow turbulent intensity	Tu = 1%
Backflow turbulent length scales	$D_H = 0.0923$ m
Bleed duct	
Outlet pressure	Gauge pressure (Pascal) = (0, 1, 1.2, 2)% of the operating pressure = 1 MPa
Backflow turbulent intensity	Tu = 1%
Backflow turbulent length scales	$D_H = 0.057$ m
STATIONARY WALL	
Shear condition	No slip

4.5. Computational flow steps

– **First step,** flow domain was generated using Gambit, then meshed with quadratic-mesh. Mesh was refined with elements from 1985–4782. Velocity and pressure criteria was set at the inlet and outlets respectively, axi-symmetry and no-slip wall conditions were applied. The fluid is an air type specification, the mesh was later exported to Fluent for simulation and analysis.

– **Second step,** further analysis was done in Fluent, the grid was resized and tested. A 2-D axi-symmetric technique, pressure based solving approach and, fluid flow parameter for air were selected. RNG k- ϵ model was applied. The inlet velocity of 60 m/s at temperature 500 K was applied.

Turbulence intensity of 1%, 3% and 5% based on inlet flow diameter were applied and atmospheric pressure type was specified at the outlet. First order upwind scheme was chosen. Convergence requirement was set at 10^{-6} and iterated.

5. Results and discussion

This section provides an overview of the conclusions drawn from the CFD analysis of the two dimensional VCD. To improve the diffuser's efficiency, various alterations on the geometry were made and experimented. Bleed rates for the VCD have been found to be between 0%, 1%, 1.2% and 2%.

5.1. Screening test results

The effectiveness of the VCD with the bleed configuration was checked using the following parameters, radial flow speed profiles at the inlet, middle and exit planes, static pressure recovery, diffuser efficiency, and diffuser total pressure loss.

Identifying the vortex fence placement and dimension that would produce the best diffuser effectiveness and the lowest pressure loss at practical suction rates was the first phase of the test process. Following this, the geometry that passed these tests was then assessed in light of the stated performance criteria. The values of Y and X shown in Fig. 1 above was altered in order to assess the impact of the bleed configuration on the diffuser performance. Table 3 includes the diffuser static pressure rise and reattachment length, L_R at 1% bleed rate, and it provides the conclusion of the investigation performed. The rise in static pressure along the center line for different axial gaps X with constant radial gaps Y is shown in Fig. 7–9.

The behavior or the change in static pressure along the center line may be described as follows: It begins with a fall of the static pressure across the inlet length, later the fluid at the diffuser neck begins to experience a rise in pressure caused by the abrupt expansion of the VCD's outflow space. Figure 10 shows the static pressure rise for different values of the distance, Y with fixed values of distance, X at tested maximum value, X = 0.015 m, we can observe that the static pressure increases as the radial gap Y decreases with increase in axial gap X. The pressure recovery improves as a result of this rise in static pressure, which is vital when designing a VCD. For values of X = 0.015 m and Y = 0.0025 m, the VCD performed well in the static pressure rise and reattachment length, L_R compared to other models values. The symbol (*) in Table 3 confirms the dimensions that were selected for the overall VCD design and were used for further analysis and the report discussed in this paper.

Table 3. Effect of suction chamber geometry on diffuser performance (exit rake position $L = 0.4$ m)

Model	Axial gap, X [m]	Radial gap, Y [m]	Inlet Mach number, M	Static pressure rise [Pa]	Reattachment length, L_R [m]	Bleed rate [%]
1	0.0045	*0.0025	0.133	-1283	0.3875	1.0
2	0.010	↓	0.133	-1035	0.3840	↓
3	*0.015	↓	*0.133	*-750	*0.3650	↓
4	0.0045	0.0045	0.133	-1204	0.4000	1.0
5	0.010	↓	0.133	-1002	0.3850	↓
6	0.015	↓	0.133	-772	0.3740	↓
7	0.0045	0.0085	0.133	-1049	0.4000	1.0
8	0.010	↓	0.133	-853	0.3863	↓
9	0.015	↓	0.133	-850	0.3862	↓

* – Final geometry chosen

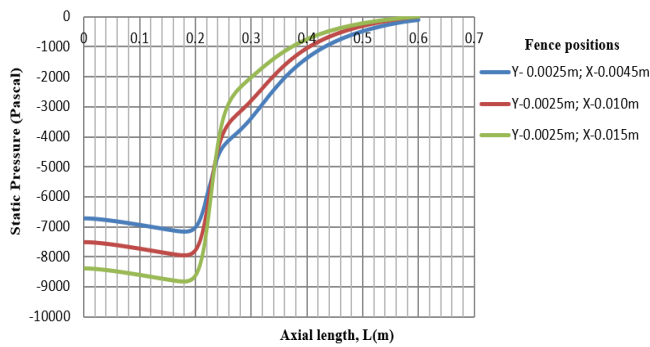


Fig. 7. Difference in static pressure rise for different values of axial gap X for fixed radial gap $Y = 0.0025$ m

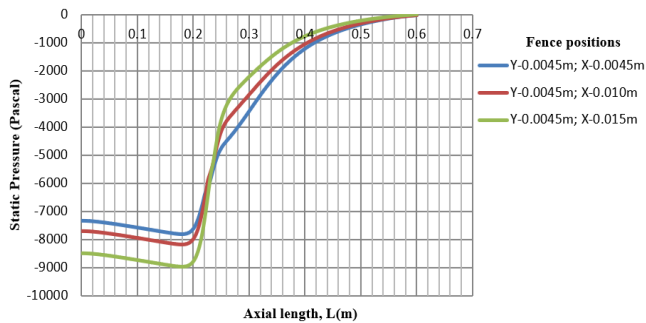


Fig. 8. Difference in static pressure rise for different values of axial gap X at fixed radial gap $Y = 0.0045$ m

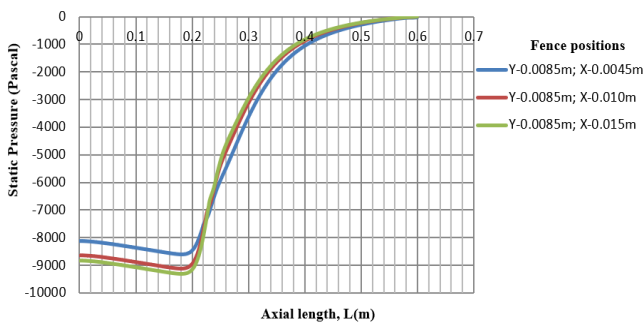


Fig. 9. Difference in static pressure rise for different values of axial gap X at fixed radial gap $Y = 0.0085$ m

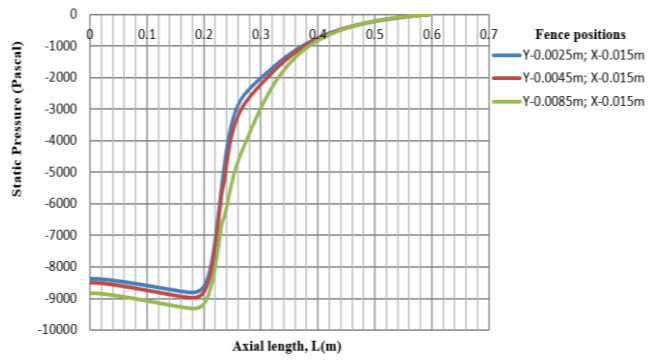


Fig. 10. Difference in static pressure rise for different values of radial gap Y for fixed axial gap X (for maximum axial gap tested $X = 0.015$ m)

5.2. Graphical representation of re-attachment length

The graphical reattachment length, L_R is described in Fig. 11–14. The reattachment length is determined by plotting the x-wall shear stress along the line lying close to the wall from the step. The reattachment length corresponds to the axial length at which the shear stress changes sign from negative to positive.

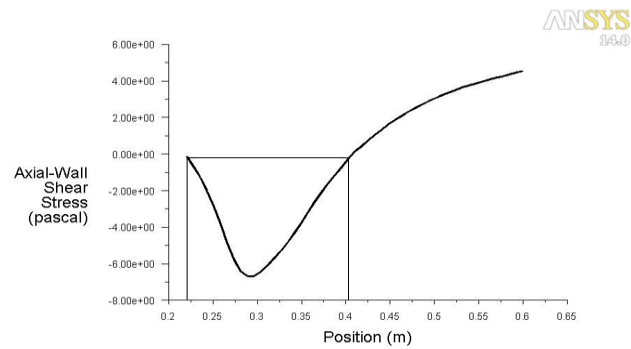


Fig. 11. Graphical representation of Re-attachment length for VCD without bleed configuration

Note that Fig. 11 is direct plot by the ANSYS software while the plots shown in Fig. 12–14 were generated using excel after exporting the corresponding result data from ANSYS, this way it was possible to plot and compare for different positions of the bleed slot and that is why in Fig. 12–14 axis starts from 0.0 and not from 0.2 as in 11.

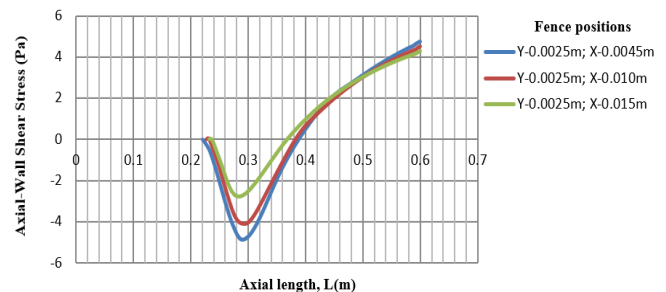


Fig. 12. Graphical representation of Re-attachment length, L_R at varying axial distance values of X at fixed radial distance $Y = 0.0025$ m

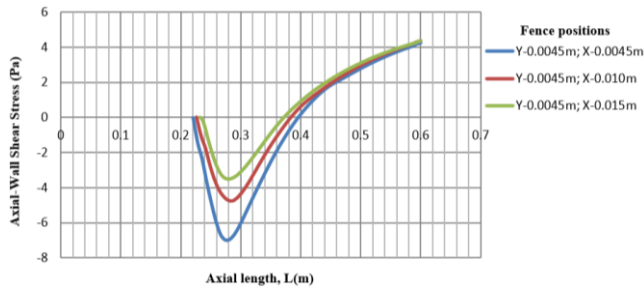


Fig. 13. Graphical representation of Re-attachment length, L_R at varying axial distance values of X at fixed radial distance $Y = 0.0045$ m

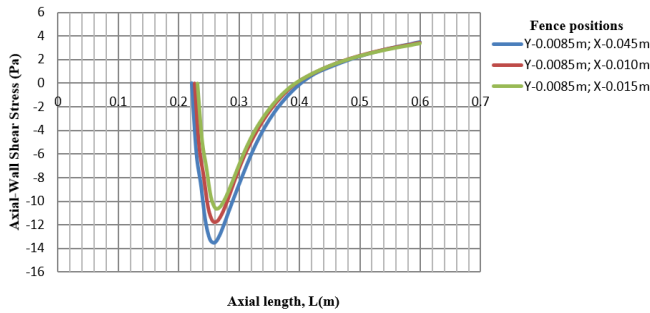


Fig. 14. Graphical representation of Re-attachment length, L_R at varying axial distance values of X at fixed radial distance $Y = 0.0085$ m

5.3. Conclusions drawn from the finalized vortex chamber design

This chapter presents the performance obtained with the final vortex chamber configuration. The factors listed below were additionally used to evaluate the VCD effectiveness:

- Pressure recovery coefficient:

$$C_p = \frac{P - P_1}{\frac{1}{2} \rho V_1^2} \quad (14)$$

where, P_1 and V_1 are pressure and average velocity inlet reference section.

P represents the static pressure at the location where the pressure coefficient is calculated.

- Ideal pressure recovery coefficient

$$C_{pi} = 1 - \left(\frac{1-B}{AR} \right)^2 \quad (15)$$

$$B = \frac{\dot{m}_b}{\dot{m}_1} \quad (16)$$

where B represents the bleed fraction, AR is the aspect ratio, \dot{m}_b and \dot{m}_1 is the mass flow rate at the bleed duct and inlet respectively

- Diffuser efficiency:

$$\eta = \frac{C_p}{C_{pi}} \quad (17)$$

- Pressure loss coefficient:

$$K = C_{pi} - C_p \quad (18)$$

5.4. Static pressure gradients across the VCD's center line

The outcome of the VCD experiments with no bleed configuration and that of 0%, 1%, 1.2%, and 2% bleed is shown in Fig. 15. In this figure we can observe the initial

decrease of static pressure across the primary duct (region a to b), there after the fluid starts to experience static pressure rise because of an abrupt expansion of the flow area (region b to c), the plot illustrates that when the bleed percentage rise, the static pressure rises as well. The part c to d is the vortex stabilization expression and at this stage, more increase in bleed would not have a significant effect on the VCD effectiveness. The situation associated with point c is known as the point of lowest bleed required, therefore the conclusion is that, for this particular VCD geometry the minimum bleed required for its proper performance is at bleed rate 2% at axial length, $L = 0.3$ m.

5.5. Pressure coefficient (C_p)

In fluid dynamics, a dimensionless number called the pressure coefficient is used to characterize the range of pressure present inside a flow field. Any location in a field of fluid motion has a different pressure coefficient. Figure 16 depicts an illustration of the pressure coefficient across the VCD center line for various bleed rates (0%, 1%, 1.2%, and 2%). As the fluid travels, the pressure coefficient rises, although at the beginning it is nearly constant.

The wall pressure coefficient (C_p), near the step corner, is negative, low, and relatively constant. It increases steadily downstream to a favorable level close to the point of reattachment. The conclusion is that the pressure coefficient rises as the bleed rates is increased.

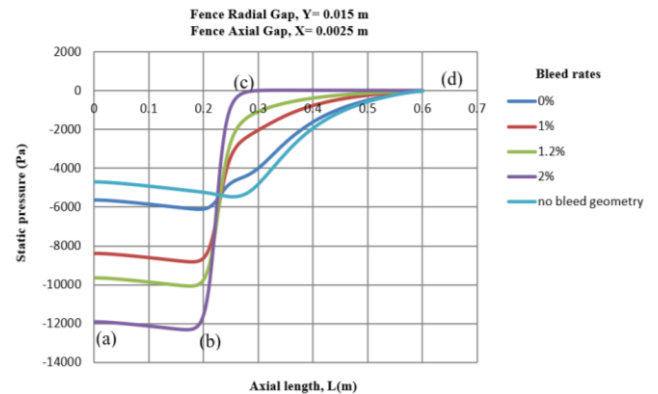


Fig. 15. Variation of static pressure rise for various bleed rates

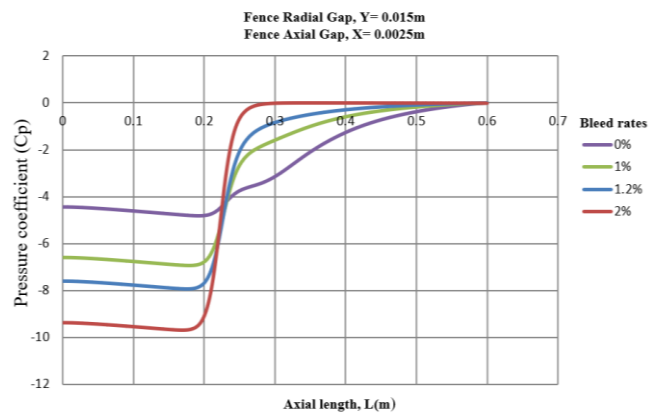


Fig. 16. Variation of pressure coefficient along the center line for various bleed rate

5.6. Static pressure contours at different bleed values

In general the static pressure varies along the length of both diffusers. Static pressure recovery is an important characteristics of an expansion diffuser. The flow pattern of static pressure for VCD with no bleed configuration and for various bleed rates are described in Fig. 17–21 respectively. For VCD without bleed configuration, Fig. 17, we can observe the gradual increase of static pressure and the region of highest static pressure recovered is at the exit of the diffuser. For the VCD with bleed rates, we can observe the region of lowest static pressure recovered mostly in the vortex chambers. In conclusion, the static pressure increases with increase in bleed rates.

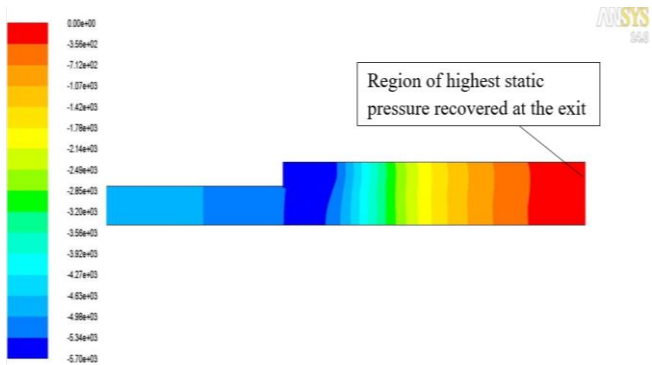


Fig. 17. Visual colors of static pressure (pascal), for VCD with no bleed configuration

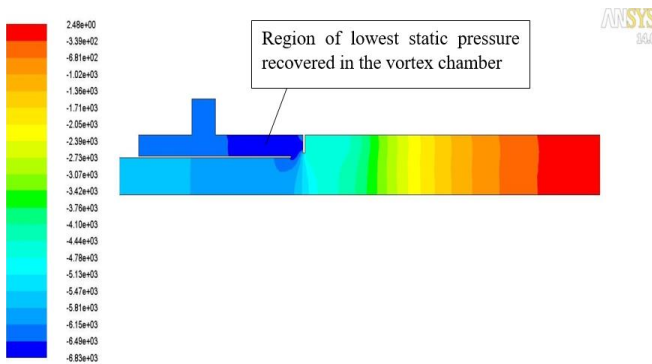


Fig. 18. Visual colors of static pressure (pascal) at 0% bleed

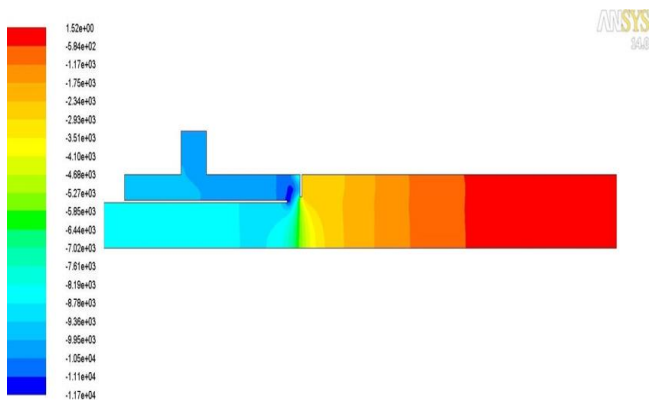


Fig. 19. Visual colors of static pressure (pascal) at 1% bleed

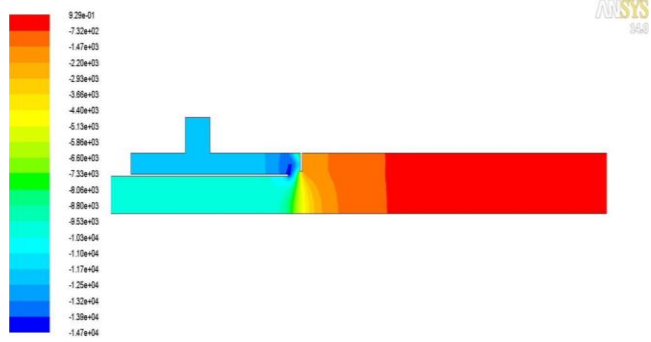


Fig. 20. Visual colors of static pressure (pascal) at 1.2% bleed

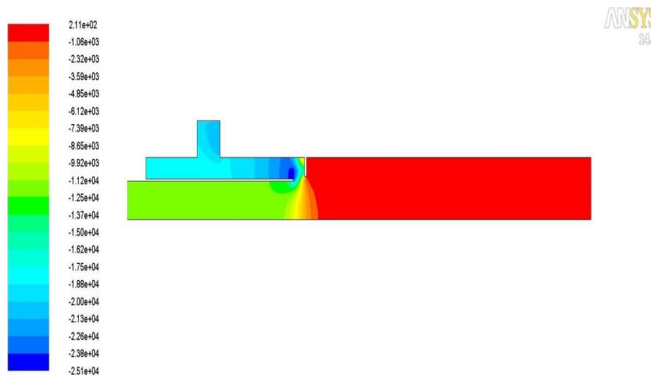


Fig. 21. Visual colors of static pressure (pascal) at 2% bleed

5.7. Streamlines of velocity magnitude

Observations were made on the recirculation and separation region. It was observed that flow separation occurred below the step boundary and free shear layer formed behind the flow separation zone as described by the streamlines of velocity magnitude in Fig. 22–25 for VCD without bleed configuration and with a bleed of 1%, 1.2% and 2% respectively. Included are the reattachment lengths, L_R , we can observe from the streamlines that the reattachment length, L_R decreases with increase in bleed rates. The more the separation reduces the more pressure is recovered.

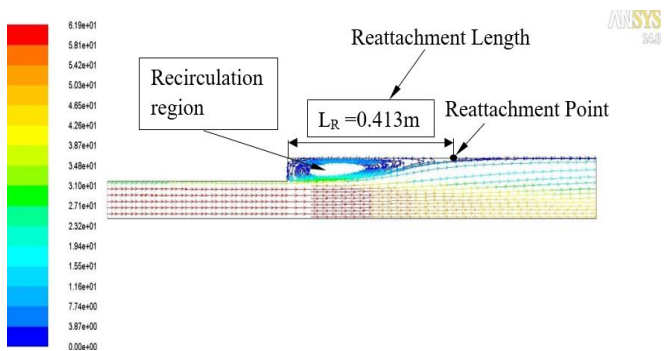


Fig. 22. Velocity magnitude (m/s) streamlines, for VCD with no bleed configuration

Rectangular region is characteristic of stationary flow. In the real flow, this vortex changes its shape and can periodically disappear, run down the stream, generating again in the corner.

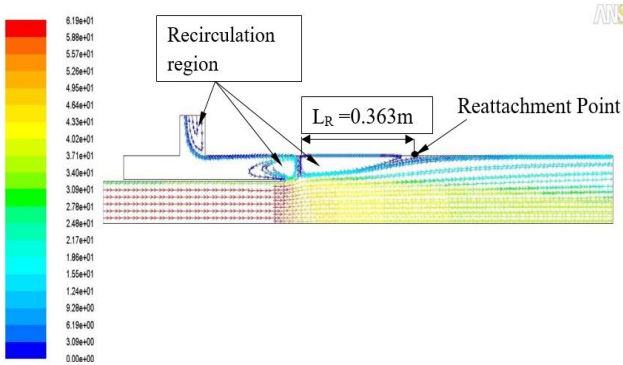


Fig. 23. Velocity magnitude (m/s) streamlines at 1% bleed

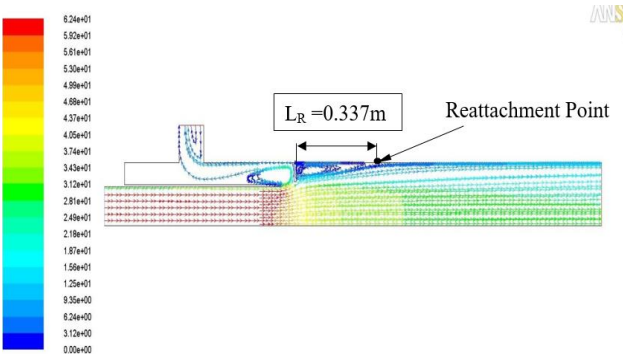


Fig. 24. velocity magnitude (m/s) streamlines at 1.2% Bleed

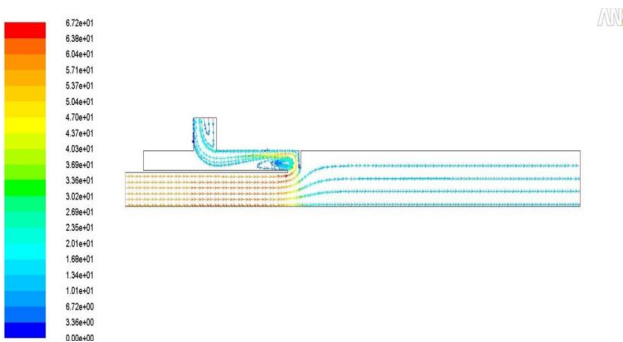


Fig. 25. Velocity magnitude (m/s) streamlines at 2% bleed, no boundary layer separation. Flow entered the vortex chamber mostly from the main stream

5.8. Variation of velocity magnitude along the center line of the VCD

Figure 26 describes the result of variation of velocity along the center line with a bleed of 0%, 1%, 1.2% and 2%, applied at the step corner. The flow behavior here can be characterized as follows: First was the acceleration of velocity along the inlet length, and later the fluid at the throat starts to display a decrease in velocity due to sudden enlargement of flow area of the VCD resulting in the formation of wall recirculation zone (see Fig. 22). In Fig. 26 we can observe that the higher the bleed the lower it is the velocity magnitude.

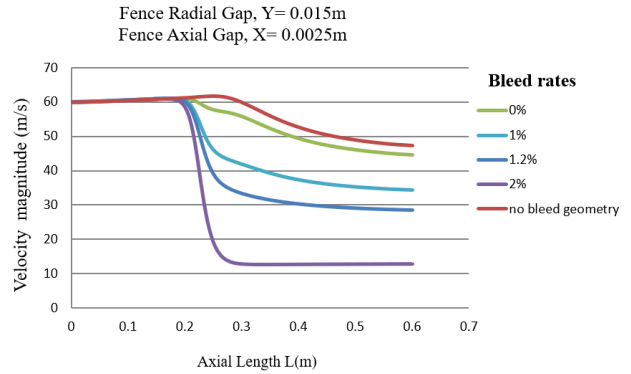


Fig. 26. Variation of velocity along the center line for different bleed rates

5.9. Radial profiles of velocity at inlet, intermediate and outlet planes

Figure 27 depicts the distribution of radial velocity at the inlet plane for different bleed levels, we can observe that at the inlet plane the bleed rates did not affect the flow velocity, the flow is uniform and fully turbulent for all bleed rates and inside the wall there is a favorable gradient i.e. $dU/dx > 0$, $dp/dx < 0$ and no separation. At the mid plane, radial length, $L = 0.03$ m we can observe in Fig. 28 that the flow separated from the wall for all bleed rates except for bleed rate 2% which is the minimum percentage bleed rate required. The separation is an indication of unfavorable pressure slope, or $dp/dx > 0$. At the exit plane we can observe in Fig. 29 that the flow is fully reattached to the wall for all bleed rates indicating that there is a zero pressure gradient at the wall i.e. $dU/dx = 0$, $dp/dx = 0$ and no separation.

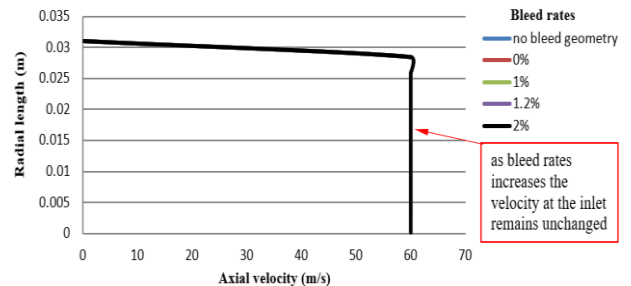


Fig. 27. Turbulent flow, radial velocity plot at the inlet plane with different bleed rates

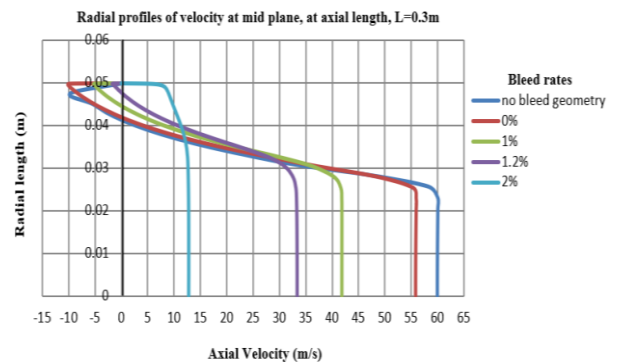


Fig. 28. Velocity radial profiles with different bleed rates at the midplane

Separation occurred except for the bleed rate 2%, which is the minimum percentage bleed rate required for this particular VCD geometry.

1.2% are presented respectively. Generally the temperature in both geometries did not increase significantly, their orders of magnitude ranges from 500 K (initial condition) to 502 K which is not very high, it is suitable for the considered geometries.

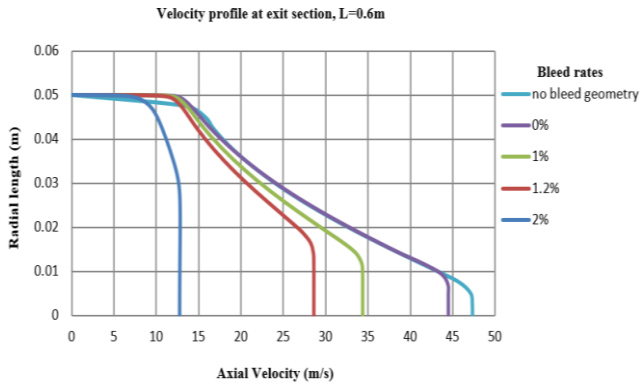


Fig. 29. Outlet plane radial velocity plot for different bleed rates

5.10. Velocity magnitude flow patterns at various bleed rates

Figures 30–34 depict the contour patterns of velocity magnitude for VCD with no bleed configuration and with a bleed of 0%, 1%, 1.2% and 2% respectively.

The contours show the weight of gradual decrease of velocity, from red (the highest value) to blue the lowest value.

In Fig. 30 the blue color close to the step corner tells the extent of boundary layer separation. The flow decreases gradually as it passes the throat due to sudden enlargement of flow area of the VCD resulting in the formation of wall recirculation region.

In Fig. 31–34 we can observe the rapid flow of air through the bleed slot as the bleed rates increases respectively. The highest rapid fluid flow through the bleed slot is observed at bleed rate 2% (see Fig. 34), this is the minimum bleed rate required for this particular VCD geometry, further increase in bleed rate greater than 2% may affect the VCD’s effectiveness in terms of static pressure recovery.

In summary, observation made is that, the diffuser incorporating the bleed geometry performed better in reducing the velocity at the exit. Due to this decrease in velocity the pressure recovery at the exit improves which is important when designing a vortex controlled diffuser.

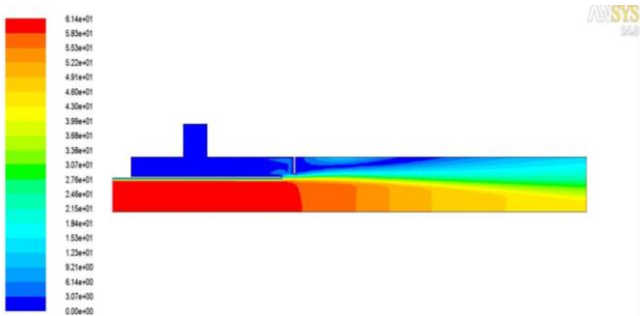


Fig. 31. Velocity magnitude (m/s) patterns at 0% Bleed

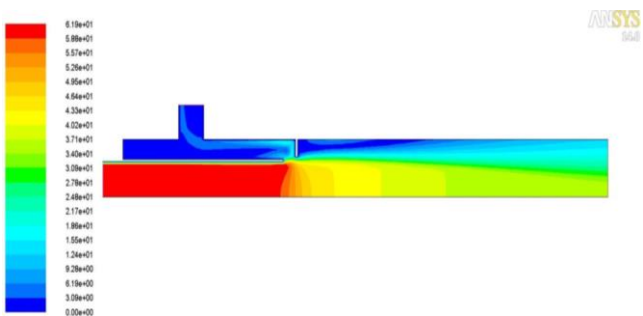


Fig. 32. Velocity magnitude (m/s) patterns at 1% bleed

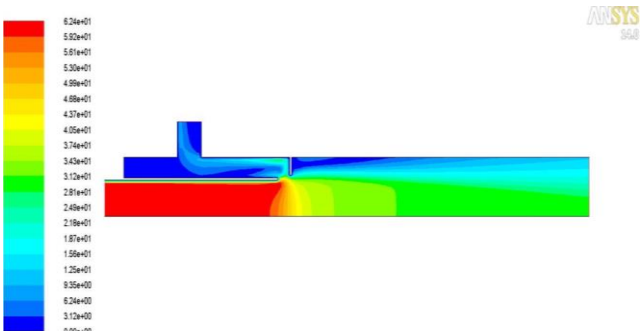


Fig. 33. Velocity magnitude (m/s) patterns at 1.2% bleed

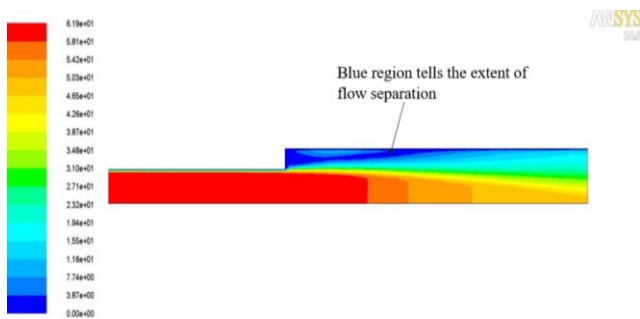


Fig. 30. Velocity magnitude (m/s) patterns with respect to the vortex controlled diffuser with no bleed configuration

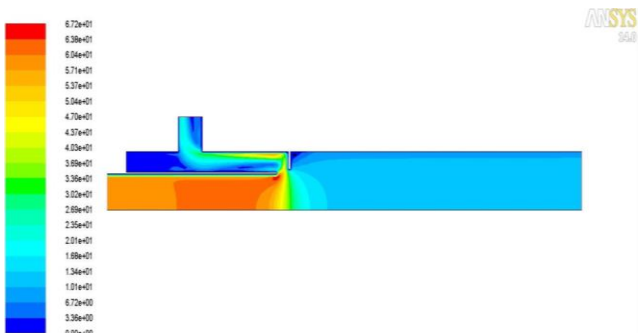


Fig. 34. Velocity magnitude (m/s) patterns at 2% bleed

5.11. Static temperature flow patterns

In the flowing figures static temperature rise for the VCD without bleed geometry and with a bleed of 1% and

In Fig. 35 the temperature rises gradually after it passes the throat, the order of magnitude is greater close to the step corner and the diffusing wall. In Fig. 36 and 37 we can observe the highest order of temperature magnitude in the vor-

tex chamber and close to the recirculation region where it is observed to be low velocity region (Bernoulli's principle).

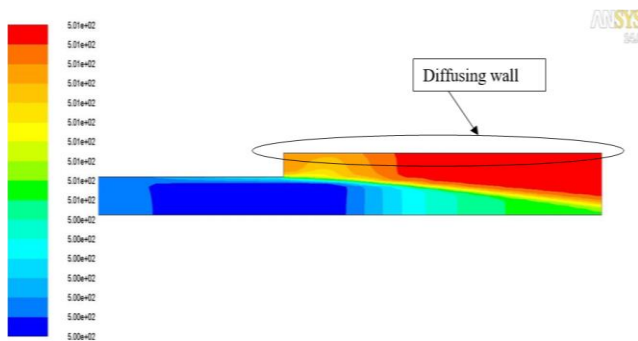


Fig. 35. Static temperature (k) patterns, with respect to the vortex controlled diffuser with no bleed configuration

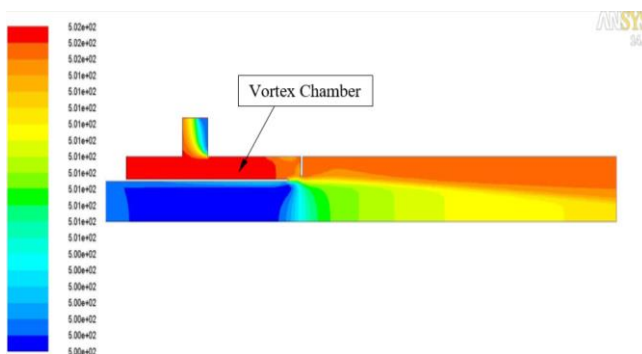


Fig. 36. Static temperature (k) patterns at 1% bleed

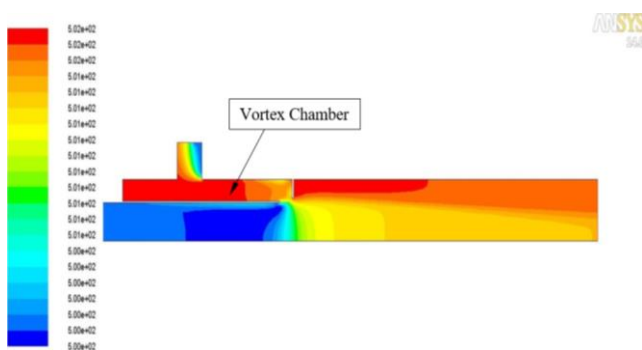


Fig. 37. Static temperature (k) patterns at 1.2% bleed

6. Summary and conclusions

A 2-D VCD effectiveness modeling has been conducted in the present study. The dimensions of Y and X shown in Fig. 1 were altered to check the efficiency of the VCD with bleed configuration. The final goal was to increase the pressure recovery inside the VCD by relieving pressure through the bleed slot.

Gambit software was used for the flow domain and mesh generation, and ANSYS FLUENT for flow modeling, applying the compressible RANS model, and RNG based $k-\epsilon$ for vortex flow.

Parameters like static pressure recovery, bleed fraction, position of bleed slot were observed and compared to VCD with no bleed configuration and below characteristics were found:

- When bleed is applied, the VCD acts differently from the VCD with no bleed configuration in relation to changes in total pressure inside fluid domain.
- With fixed velocity 60 m/s and specified aspect ratio, the static pressure rise improves as the bleed rates gets higher.
- The favorable dimension for the bleed fence for this particular VCD geometry is at distance, $X = 0.015$ m and $Y = 0.0025$ m close to the step corner of the VCD.
- The VCD without bleed configuration did not reduce the velocity magnitude at its exit, but the chosen geometry for the VCD with the bleed configuration performed better by decreasing the exit velocity from 60 m/s (assumed inlet velocity) to 41 m/s at 1% bleed and 10.5 m/s at 2% bleed.
- When air is delivered to the combustion chamber, the air bleed regulates the strength of the vortex that is created in the vortex chamber, which in turn regulates the pace at which air diffuses.

Nomenclature

VCD vortex-controlled diffuser
 RANS Reynolds averaged Navier-Stokes
 AR aspect ratio
 L_R reattachment length

RNG Re-Normalisation Group (turbulence flow model)
 CFD computational fluid dynamics
 C_p pressure coefficient

Bibliography

- [1] Adkins RC, Matharu DS, Yost JO. The hybrid diffuser. ASME Technical Paper 1980;80-GT-136. <https://doi.org/10.1115/80-GT-136>
- [2] Adkins RC. A short diffuser with low pressure loss. J Fluids Eng. 1975;97(3):297-302. <https://doi.org/10.1115/1.3447306>
- [3] ANSYS CFX solver theory guide. Release 14. ANSYS Inc. Canonsburg 2011.
- [4] Chakrabarti S, Rao S, Mandal DK. Numerical simulation of the performance of a sudden expansion with fence viewed as a diffuser in low Reynolds number regime. J Eng Gas Turbines Power. 2010;132(11):114502. <https://doi.org/10.1115/1.4000800>
- [5] Cockrell DJ, Markland E. A review of incompressible diffuser flow: a reappraisal of an article by G. N. Patterson entitled 'Modern diffuser design' which was published in this

- journal twenty-five years ago. *Aircr Eng Aerosp Tec.* 1963; 35(10):286-292. <https://doi.org/10.1108/eb033790>
- [6] Ghose P, Datta A, Mukhopadhyay A. Effect of prediffuser angle on static pressure recovery in flow through casing-liner annulus of a gas turbine combustor at various swirl levels. *J Thermal Sci Eng. Appl.* 2016;8(1):1-7. <https://doi.org/10.1115/1.4030734>
- [7] Gorla RSR, Khan AA. *Turbomachinery: Design and theory.* 1st ed. CRC Press, Taylor and Francis Group. Boca Raton 2003. <https://doi.org/10.1201/9780203911600>
- [8] Heskestad G. A suction scheme applied to flow through sudden enlargement. *J Basic Eng.* 1968;90(4):541-552. <https://doi.org/10.1115/1.3605188>
- [9] Heskestad G. An edge suction effect. *AIAA J.* 1965; 3(10):1958-1961. <https://doi.org/10.2514/3.3294>
- [10] Heskestad G. Further experiments with suction at a sudden enlargement in a pipe. *J Basic Eng.* 1970;92(3):437-447. <https://doi.org/10.1115/1.3425025>
- [11] Klein A. Characteristics of combustor diffusers. *Prog Aerosp Sci.* 1995;31(3):171-271. [https://doi.org/10.1016/0376-0421\(95\)00006-K](https://doi.org/10.1016/0376-0421(95)00006-K)
- [12] Lefebvre AH, Ballal DR. *Gas turbine combustion. Alternative fuels and emissions.* 3rd ed. CRC Press, Taylor and Francis Group. New York 2010. <https://doi.org/10.1201/9781420086058>
- [13] Mandal DK, Bandyopadhyay, Chakrabarti S. A numerical study on the flow through a plane symmetric sudden expansion with a fence viewed as a diffuser. *Int J Eng Sci Tech.* 2011;3(8):210-233. <https://www.ajol.info/index.php/ijest/article/view/80186>
- [14] Mandal DK, Manna NK, Bandyopadhyay S, Biswas BP, Chakrabarti S. A numerical study on the performance of a sudden expansion with multisteps as a diffuser. *Int J Appl Mech.* 2011;3(4):779-802. <https://doi.org/10.1142/S1758825111001238>
- [15] Schäfer F, Breuer M, Durst F. The dynamics of the transitional flow over a backward-facing step. *J Fluid Mech.* 2009; 6233:85-119. <https://doi.org/10.1017/S0022112008005235>
- [16] Versteeg HK, Malalasekera W. *An introduction to computational fluid dynamics.* 2nd ed. Pearson. Prentice Hall, Glasgow 1995. http://ftp.demec.ufpr.br/disciplinas/TM701/Versteeg_Malalasekera_2ed.pdf
- [17] White FM. *Viscous fluid flow.* 3rd ed. McGraw Hill. New York 1974. http://paginapessoal.utfpr.edu.br/fandrade/teaching/files/Viscous_Fluid_Flow_3rd_White.pdf
- [18] Wilcox DC. *Turbulence modelling for CFD.* 3rd ed. DCW Industries. California 2006. https://cfd.spbstu.ru/agarbaruk/doc/2006_Wilcox_Turbulence-modeling-for-CFD.pdf
- [19] Xing F, Su H, Chan S, Xu L, Yu X. Optimization study of the dump diffuser in gas turbine to reduce pressure loss. *Int J Aerospace Eng.* 2018;1-14. <https://doi.org/10.1155/2018/6070782>

Emeka Gaius Chijioke, DEng. – Faculty of Power and Aeronautical Engineering, Warsaw University of Technology, Poland.
e-mail: emekachijioke9@gmail.com



Prof. Andrzej Teodorczyk, DSc., DEng. – Faculty of Power and Aeronautical Engineering, Warsaw University of Technology, Poland.
e-mail: andrzej.teodorczyk@pw.edu.pl

